A Probabilistic Asteroid Impact Risk Model

Donovan L. Mathias[a], Lorien F. Wheeler[b], Jessie L. Dotson[c]

[a] NASA Ames Research Center, MS 258-5, Moffett Field, CA 94035, donovan.mathias@nasa.gov
[b] CSRA, NASA Ames Research Center, MS 258-6, Moffett Field, CA 94035, lorien.wheeler@nasa.gov
[c] NASA Ames Research Center, MS 244-30 Moffett Field, CA 94035, jessie.dotson@nasa.gov

Abstract

Asteroid threat assessment requires the quantification of both the impact likelihood and resulting consequence across the range of possible events. This paper presents a probabilistic asteroid impact risk (PAIR) assessment model developed for this purpose. The model incorporates published impact frequency rates with state-of-the-art consequence assessment tools, applied within a Monte Carlo framework that generates sets of impact scenarios from uncertain parameter distributions. Explicit treatment of atmospheric entry is included to produce energy deposition rates that account for the effects of thermal ablation and object fragmentation. These energy deposition rates are used to model the resulting ground damage, and affected populations are computed for the sampled impact locations. The results for each scenario are aggregated into a distribution of potential outcomes that reflect the range of uncertain impact parameters, population densities, and strike probabilities. As an illustration of the utility of the PAIR model, the results are used to address the question of what minimum size asteroid constitutes a threat to the population. To answer this question, complete distributions of results are combined with a hypothetical risk tolerance posture to provide the minimum size, given sets of initial assumptions. Model outputs demonstrate how such questions can be answered and provide a means for interpreting the effect that input assumptions and uncertainty can have on final risk-based decisions. Model results can be used to prioritize investments to gain knowledge in critical areas or, conversely, to identify areas where additional data has little effect on the metrics of interest.

1. Introduction

Dramatic evidence exists to suggest extreme consequences can result when asteroids strike the Earth. Images of tree-fall in Tunguska [1], the impressive Meteor Crater [2], historical record of the Eltanin [3] ocean impact, and the K-T dinosaur extinction event [4] all represent potential impact consequences. In the 1990s, studies began to quantify the level of hazard posed by such asteroid strikes by evaluating their potential consequences and expected impact probabilities [5] [6] [7]. In 1992 the threat was considered significant enough that the U.S. Congress mandated the Spaceguard Survey to locate 90% of near earth asteroids grater than 1km in diameter [8]. The next major risk assessment was produced in 2003 [9] and in 2005 led to the George E. Brown Jr. survey to extend the search criteria down to objects 140m in diameter [10]. In 2010, the National Research Council (NRC) produced a report [11], which asserted that a search for much smaller objects was required. Then in 2013, while the world watched the flyby of asteroid 2012 DA14, a smaller asteroid only 20m in diameter—below the threshold many considered to be a threat— entered the atmosphere over Chelyabinsk, Russia and caught the attention of the world with widespread video capture of the resulting fireball. While the Chelyabinsk meteor caused no fatalities, the shockwave produced by its atmospheric breakup injured over 1000 people and caused $33 million in damage [12]. Following the Chelyabinsk event, a

number of new looks at impact risk assessment have emerged [13] [14]. In the current paper, further advances to impact risk modeling are presented.

When reviewing the literature, it is worth differentiating between the impact hazard and the impact risk. A hazard is typically considered to be a potential damage-causing event or action [15], whereas risk is defined as the consequence of an event weighted by the probability of the event occurring. Previous papers have looked at impact consequences for representative events ([16] [17] [18] [19] [20]) and collectively from a hazard perspective (e.g. [7] [5] [6]). Risk assessments have either evaluated the risk posed by known objects [21] [13]or by a statistical ensemble of hypothetical objects ([9] [11] [22] [23] [14]). Stokes performed the first real look at quantifying risk by considering a range of impactor sizes each with a single, representative set of physical properties (density, velocity, strength, etc.). Subsequent efforts have extended Stokes' approach [11] [22], but the updates largely focus on improvements in characterization of the asteroid population, and corresponding updates to the estimated impact frequency. References [9], [11], [22] all considered representative impact scenarios with an assumed set of mean asteroid and entry parameters (i.e., density, entry angle, velocity, etc.), and often, average human population distribution on Earth. As a result, the metrics used to report the risk have typically been based on annual expected casualties, i.e., the average annual casualty rate calculated based on infrequent events averaged over a long time period. Stokes [9] presented expected casualty rates, but also considered the actual population distribution and presented probability numbers describing the likelihood of affecting more than a given number of people as a function of impactor size, assuming a single representative scenario. Reinhardt [23] and Motiwala [14] both included uncertainty distributions that described the range of possible impactor characteristics as well as random impact locations. These authors both performed the risk assessment using a Monte Carlo approach and presented uncertainty distributions of outcomes. Motiwala [14] included the atmospheric entry and breakup process explicitly in the risk modeling whereas Reinhardt utilized parametric equations to estimate the ground hazards for each scenario.

The current work extends the approach implemented in [14] and embeds physical meteor entry models into a probabilistic risk assessment. Single-body equations are explicitly integrated for each impact case within the Monte Carlo framework so that a more faithful treatment of entry physics can be associated with the consequence assessment. This allows explicit representation of the physical processes that occur during entry, increasing the fidelity of the results, and allows for the examination of the sensitivity of the results to the input assumptions. The following sections will describe the risk model framework and the physical models currently incorporated. While the model can be used to assess the threat of impact in a variety of scenarios, including the case of a specific object, this paper shows ensemble risk results for a range of stochastic impact scenarios. These results include the distributions of damage likelihoods given the input assumptions, and illustrate how the distributions provide much more information than average expected values. As an example, the results are used to define a minimum asteroid size that would constitute a considerable threat, based on a hypothetical risk tolerance. Finally, we will demonstrate how the current risk model can be used to examine how this hypothetical threat size changes based on the assumptions and uncertainties in the available information.

2.   Probabilistic Asteroid Impact Risk Model

The PAIR model presented is an extension of the model first described in [14]. The current version of the model has been extended to include an improved breakup model that estimates burst altitudes from specific energy deposition rates for a variety of fragmentation characteristics, a thermal radiation damage model, and a more flexible scenario generation frontend that allows input parameters to be defined using a variety of uncertainty distributions. Currently, the model execution consists of three phases: impact scenario generation, impact consequence modeling, and risk analysis of the combined hazard results. The model generates sets of potential impact scenarios, performs physical modeling of the asteroid's entry, breakup, and ground damage for each case, computes the population affected by each modeled impact, and then quantifies the aggregate risks by weighting the relative damage probabilities with corresponding impact frequency estimates.

2.1   Impact Scenario Generation

The scenario generator consists of a Monte Carlo framework where distributions of input variables are defined and sampled to produce a specified number of impact cases for analysis. The input variables include asteroid properties (such as size, density, and strength), impact parameters (such as velocity, entry angle, impact location), and some modeling parameters (such as ablation coefficient and luminous efficiency) that can be varied to capture either modeling uncertainty or ranges of potential physical variations. Each parameter can be held constant, treated as uniformly or normally distributed, or given a custom distribution.

The asteroid size can either be assigned directly through a diameter distribution, or can be determined from sampled H-magnitude and albedo values. As will be discussed in the breakup modeling section, the asteroid strength is represented using an initial aerodynamic breakup strength, along with a fragment strength scaling parameter that controls the successive fragmentation rate once breakup begins. The ablation coefficient varies the mass ablation rate used to compute atmospheric energy deposition in the entry-modeling phase, and the luminous efficiency is used to estimate the potential thermal radiation.

Upon execution, the scenario generator samples the appropriate distributions and generates a list of the user specified number of impacts. The specific input distributions used for current assessment results are presented in Section 3 below.

2.2   Atmospheric Entry and Breakup Modeling

For each impact scenario, the asteroid's entry and breakup are modeled to estimate an airburst altitude or ground impact based on the energy deposited in the atmosphere through drag and ablation. The energy deposition is modeled using the fragment-cloud

model (FCM) from [24], which combines a discrete, progressive fragmentation approach with releases of dispersing debris clouds. This approach is able to represent/reproduce the types of large flares observed in the Chelyabinsk meteor event and also allows for larger, stronger fragments to penetrate further and burst lower. A summary of the modeling approach is included here, and references [25] and [24] contain a complete discussion of the fragmentation and energy deposition models.

The entry flight dynamics are modeled by integrating the single-body equations [26]:

$$dm/dt = -0.5\rho_{air}v^3A\sigma$$
$$dv/dt = \rho_{air}v^2AC_D/m - g\sin\theta$$
$$d\theta/dt = (v/(R_E+h) - g/v)\cos\theta$$
$$dh/dt = v\sin\theta$$

where m is the mass of the asteroid, v is the velocity, θ is the flight path angle, h is the altitude, t is time from the initial interface, g is acceleration due to gravity, ρ_{air} is the local atmospheric density, R_E is the radius of the earth, A is the cross-sectional area of the object, C_D is the drag coefficient, and σ is the ablation coefficient.

The initial flight integration begins 100 km above the surface of the Earth and continues until the stagnation pressure exceeds the object's aerodynamic strength:

$$\rho_{air}v^2 > aerodynamic\ strength$$

Once the asteroid's aerodynamic strength is exceeded, the parent body is broken into a given number of individual child fragments and an aggregate debris cloud. The model allows the number of fragments and cloud mass per split to be specified at run time, with a baseline setting of two fragments and 50% cloud mass for each fragmentation event. The child fragments are treated themselves as intact bodies with an increased strength given by

$$S_{child} = S_{parent}(m_{parent}/m_{child})^\alpha$$

where S represents the strengths, m the masses, and α is the power law strength-scaling exponent. The child fragments then continue to fly until they reach their respective failure strengths and again break into the prescribed number of fragments and cloud mass. The process continues until the fragments reach the ground or become slow or strong enough to no longer reach the breakup condition. Following the approach of [27], the debris cloud mass is treated aerodynamically as a single deformable body that spreads and slows under a common bow shock. The lateral spread rate of the body's effective drag area is given by the expression [27]:

$$v_{dispersion} = v_{cloud}(3.5\rho_{air}/\rho_{cloud})^{1/2}$$

where v_{cloud} is the velocity of the debris cloud, decelerating with each integration step, and ρ_{cloud} is the density of the initial asteroid material. [28] derives a similar expression for fragment spread rates, which differs only slightly in the value of the constant being 3.0 (as

vs. 3.5) for analogous input assumptions. Laurence [29] has also studied the relative motion of fragments in hypersonic flight. The mechanics of the cloud debris dispersion are important to the energy deposition and subsequent ground damage that drives the risk. Sensitivity studies in [24] indicate that dispersion rate coefficients within the range of those from references [27] and [28], or higher, have little effect on energy deposition (for the baseline assumption of 50% cloud mass), although reducing the coefficient by more than half could lower burst altitude estimates. A thorough discussion of the energy deposition modeling can be found in [24].

As the fragments and debris clouds decelerate and ablate according to the above equations, the total loss of kinetic energy of all components is tracked and summed to estimate the energy deposited in the atmosphere per unit altitude. The point of maximum energy deposition is taken to represent the approximate burst altitude of the impact case. Figure 1 shows a sample FCM energy deposition curve and the burst altitude associated with the peak. If the asteroid fails to break up or the energy deposition rate is still increasing at ground level, then the case is considered to be a ground impact with a burst altitude of zero. The burst altitude is then used to estimate the damage areas due to blast overpressure and thermal radiation as described below.
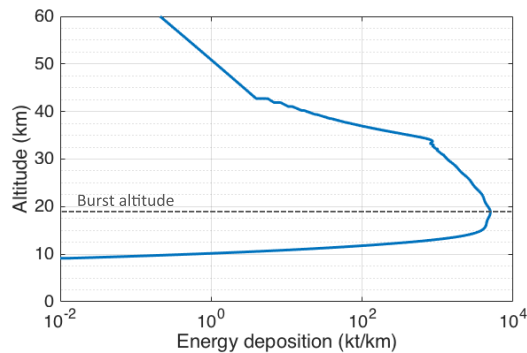

Figure 1. Energy deposition curve computed using the fragment-cloud model (solid blue line), showing burst altitude at peak (dashed line). The case shown is for a 100 m diameter asteroid with a density of 2.5 g/cc and aerodynamic breakup strength of 1 MPa entering at a velocity of 20 km/s and angle of 45° from horizontal.

2.3   Blast Overpressure Damage

Blast waves from an asteroid airburst or ground impact can cause varying levels of infrastructure damage or casualties over large areas. The PAIR model uses curve fits of nuclear test data from [27] to estimate the blast damage radius for a given burst energy and altitude. The burst altitude is based on the peak energy deposition point as described in § 2.2, and the burst energy is assumed to be equal to the full initial kinetic energy of the asteroid. While in reality the energy going into the blast will be some fraction of the deposited energy, it is not well known what energy fraction is appropriate compared to the traditionally utilized static nuclear sources. Assessments presented in [27] and [9]

assumed that all of the kinetic energy contributes to the blast for their calculations, while the assessment in [7] assumed a 50% contribution with the rest going into other energy modes such as radiation. Hills and Goda later suggested that an amount less than 100% would be appropriate [30]. However, other researchers [17] [31] have shown that a moving energy source does not act identically to the static airburst assumed in the nuclear scaling relations, and tends to produce a ground footprint that appears stronger than an equivalent static source. For this reason, putting 100% of the kinetic energy into the blast scaling relations seems to correlate better with the high fidelity simulations and is used herein to provide a bounding, worst-case assessment.

Following [9] [27] [32], the baseline ground damage area is taken as the region within which overpressure levels exceed 4 psi. The 4-psi ground damage radius, r, is estimated using the scaling relation that [27] derived from nuclear sources in [32], given by:

$$r = 2.09h - 0.449h^2 E^{-1/3} + 5.08E^{1/3}$$

where E is the impact energy, and h is the burst altitude.

2.4   Thermal Radiation Damage

In addition to blast overpressures, large bursts or impacts can release damaging levels of thermal radiation. The PAIR model adapts the model from Collins [33], which estimates the radius within which thermal radiation exceeds damage causing limits. The model computes these distances based on impact energy and a luminous efficiency parameter that defines what fraction of the energy is emitted as thermal radiation. Collins [33] notes that this parameter is poorly constrained, and cites a range of 1e-4 to 1e-2, with 0.003 taken as their assumed baseline value. For the current assessment, the luminous efficiency is sampled as an uncertain parameter for each impact case, as described in the scenario/inputs section. The original formulation from [33] assumes that the thermal radiation emanates from a fireball plume of a ground impact, and distributes the available radiation energy over the hemispherical area above the ground to determine the exposure threshold radius, r:

$$r = \sqrt{\eta E / 2\pi \Phi_i} \qquad \Phi_i = Z_i E^{1/6}$$

where r is the threshold radius from the burst or impact point, η is luminous efficiency, E is the impact energy, and Φ_i is the thermal exposure (total heating per unit area) associated with a given damage severity. The damage severity is computed for a given impact energy based on energy scaling from the corresponding thermal exposure threshold for a 1-megaton explosion, Z_i. The thermal exposure level corresponding to 3rd degree burns (Z_i = 0.42 MJ/m^2/Mt$^{1/6}$) is taken as the baseline damage area threshold, with an option to output 1st and 2nd degree burn threshold areas as well. Implicit in the formulation is the time over which the energy is radiated. As Collins points out, larger explosions radiate more energy than smaller explosions, but the time over which the energy is released is also longer. The Φ_i in the denominator of the radius expression is the result of the exposure time. All results are scaled from the 1-megaton results derived by [32].

The PAIR model extends the formulation to include airburst cases by taking the Collins hemispherical radius, r, centered at the burst altitude, h, and computing the intersecting ground radius as $R_{ground} = \sqrt{r^2 - h^2}$, accordingly. Although thermal energy would realistically be emitted spherically around the airburst, the current model maintains the hemispherical energy distribution, as an upper bound on the area, assumed in the original formulations. Practically, this bounding assumption does not skew the results, as the blast overpressure is the dominant damage-causing source.

2.5   Local Affected Population Estimates

Blast and thermal radiation damage radii are computed for each specific impact case, and the larger of the two is taken as the local damage area. The damage area is centered at the coordinates sampled for the given impact, and the local population within that area is counted as the affected population in the damage assessment. Although actual damage severities and casualty rates would fall off gradually with distance, including both survivors inside the defined damage region and some casualties occurring beyond it, the 4-psi and 3rd degree burn thresholds are assumed to provide a level of severity at which much of the population would be substantially affected by the damage or, alternately, provide a reasonable balance between survivors within and casualties without. Use of the population within a distinct damage area also allows for additional risk sensitivity analyses to be performed in the post-process phase using localized population densities.

The local populations are computed based on gridded population data from the Socioeconomic Data and Applications Center [34]. The data set used in the current assessment provides population counts within 2.5-arc-minute grid cells, based on UN-adjusted census data from the year 2000. Damage areas typically overlap portions of multiple grid cells. The fraction of the population affected in each cell is computed by dividing the cell into a user-specified number of sub-cells, and scaling the cell's population count by the fractional area of sub-cells with center points inside the damage radius. Figure 2 shows diagram of a damage area over a grid region and an example of the sub-cell areas used to compute the population fraction for a cell on the damage boundary. This gridded population count is repeated for each of the impact scenarios, using the specific computed damage area and sampled impact coordinates for each case. Results for each simulated strike are then stored and processed in the final risk assessment phase.
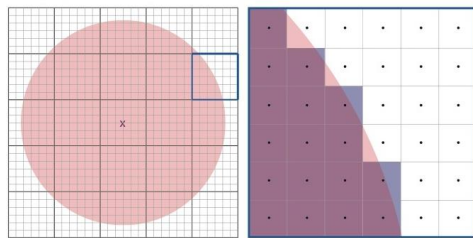
Figure 2: Notional diagram of how affected population is computed from the population grid. The figure on the left shows a damage circle (pink) over a 6x6 grid-cell region. The right-hand figure shows a close-up of one of the boundary grid cells, divided into a user-specified number of sub-cells, with the blue overlay showing the sub-cell areas contributing to the population fraction counted from within that cell.

2.6   Risk Analysis

Impact consequences are then converted into the related risk by weighting the affected population results by the likelihood of such impacts. Because the current assessment focuses on the ensemble risk rather than a specific impact scenario, the frequency of impact is determined using the general asteroid population estimates published by Harris [35]. The results provide bounding estimates on the risk, including the uncertainty around the lack of complete asteroid population knowledge, and can be used to identify how the risk uncertainty changes based on additional information about the population.

3.   Ensemble Asteroid Threat Assessment

The PAIR analysis approach described in the preceding sections is now applied to a statistical range of hypothetical impactors to establish bounds on the resulting risk. Risk will be defined via the affected population within the damage radii as described above. We will begin by discussing the uncertainty distributions used for each sampled input parameter, which were all defined based on established ranges from the literature. Model convergence is then covered to establish the number of Monte Carlo samples needed to ensure that the uncertainty in the output is driven by the input distributions and not a bias from insufficient sampling. Results will be shown using the average expected casualty metrics and compared with the full risk probability distributions enabled by the PAIR assessment approach. We will then consider the question of how small of an asteroid constitutes a significant threat to humans. This will require the introduction of a specific risk tolerance posture, and we will use the model results to answer the question in that context. Lastly, we will revisit the size-of-threat question considering the uncertainty in object size as defined by the albedo distribution. The results will illustrate how the current risk model can provide information highlighting the sensitivity of the results to the underlying assumptions and potentially identify areas where increased knowledge could improve our understanding of the threat.

3.1   Input Parameter Distributions

For this assessment case, 30 million stochastic impacts were modeled. Each available input parameter was allowed to vary freely from case to case, sampled randomly from a baseline set of uncertainty distributions derived from the literature. The distributions and ranges are described below and shown in Figure 3.

Size: Asteroid sizes were determined based on sampled H-magnitude and albedo values. The H-magnitude was sampled uniformly from 20 to 30, and the albedo was sampled from the NEOWISE distribution [36]. The diameter was then computed from the sampled values as: $D = (1.326 \times 10^6) \times 10^{-H/5} / \sqrt{p_v}$, where D is in meters, H is the absolute magnitude,

and p_v is the albedo [37]. This resulted in asteroid diameters ranging from 1.5 m to 1.33 km for the current data set, with more cases sampled at smaller sizes and over 90% of the cases having diameters under 300 m. This size range was chosen because it is appropriate for the specific applications discussed in §3.3 and §3.4.

Density: Current estimates of asteroid densities remain notably uncertain and debatable, since measurements of pre-entry asteroid compositions are extremely difficult, and meteorites that survive to the ground are not necessarily representative of large asteroid bodies as a whole. The distribution of measured asteroid densities is very asymmetrical and sensitive to selection effects. However, the distribution of macroporosities derived from asteroid density measurements is symmetrical and relatively insensitive to selection choices. Our nominal input density distribution is based on the density distribution of meteorites and modified by a likely macro-porosity distribution. The meteorite density distribution was calculated based on measured density distributions of different meteorite classes [38] and the relative fraction of each class by falls [39]. The macroporosity distribution was developed based on the values tabulated by Carry [40]. There were 97 objects with density measurements whose relative uncertainty was ≤ ±50% and with macroporosities greater than zero. Based on that population of objects, we used a Gaussian distribution with a mean of 34% and sigma of 18% to model the macroporosity.

Strength: The initial aerodynamic breakup strength was sampled from a logarithmic distribution from 0.1 to 10 MPa [41]. Published estimates of fragment strength scaling exponent values vary widely from as low as 0.03 [42] to 0.57 [43]. Based on the summary by [41], a uniform distribution between 0.1 and 0.3 was used for the current assessment. Sensitivity studies of FCM fragmentation parameters have also shown these ranges to produce reasonable variations of energy deposition curves to represent uncertainties in breakup mechanics due to asteroid composition [24].

Velocity: This assessment uses an impact velocity distribution derived by Greenstreet et al [44]. [44] simulated near-Earth asteroid populations by modeling the injection of objects into the near-Earth region due to resonances, utilizing an approach very similar to Bottke et al [45]. Due to increases in computing power, the Greenstreet model was able to simulate 6 times more objects with finer time-step resolution, permitting improved statistics and improved modeling of high-speed planetary encounters.

Entry angle: Entry angles are sample from a cosine distribution that weights entry angle probabilities toward 45°. Studies have shown 45° to be the most probable entry angle, with vertical or very shallow entries much less likely [46]. The distribution is given by $\theta° = (90°/\pi)cos^{-1}(2U − 1)$, where U is a random number sampled uniformly between 0 and 1.

Impact location: The nominal model inputs are to randomly select longitude and latitude so that the entire area of the globe is evenly sampled. Gallant et al [47] used the debiased NEO population model of [45] to examine the spatial distribution of objects impacting earth, and found that, averaged over the year, there was less than a 5% latitudinal variation after correcting for even areal coverage.

Ablation parameter: The ablation coefficient, σ, used in the flight integration was sampled from a logarithmic distribution between 3.5e-10 7e-8 kg/J. This broad range was based on review of various literature sources [48] and is intended to represent the large uncertainty in this parameter.

Luminous efficiency: The luminous efficiency parameter used in the thermal radiation model was also sampled logarithmically from a large, highly uncertain range found in the literature. A range from 3e-4 to 3e-2 was selected based on the 1e-4 to 1e-2 range from [33], but shifted slightly to center logarithmically on the nominal 0.003 value from reference [33].
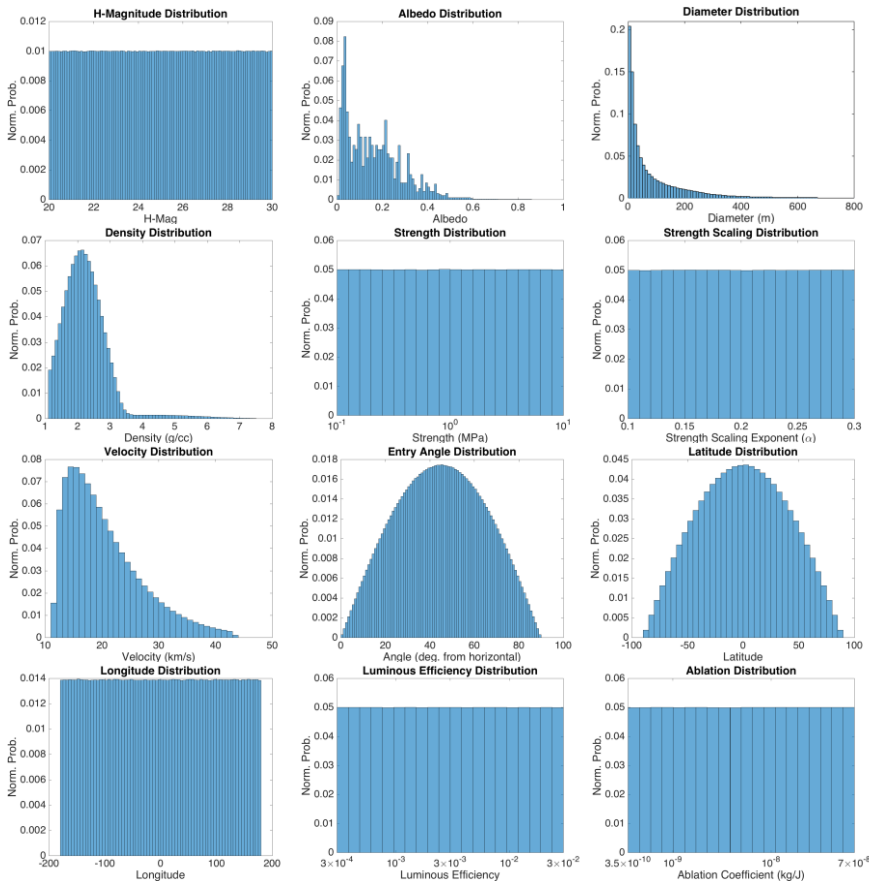
Figure 3: Histograms of the input parameter distributions sampled to produce the impact cases for the presented risk assessment.

3.2   Convergence

Given the input distributions, sufficient scenarios must be run so that the resulting statistical distributions are meaningful, covering the full range of potential outcomes thoroughly enough that the results do not continue to change with additional cases. For the current assessment, 30 million impact cases were run, with varied asteroid properties, entry parameters, impact locations, and model parameters all sampled from the distributions described in the previous section. The various damage areas produced by the range of asteroid parameters sampled converges quickly to an average value within a fairly small number of cases. The location of impact, however, causes the results to vary significantly; impacts in the ocean infrequently cause damage while similar impacts in large metropolitan regions result in large affected populations. Therefore, the affected population count serves as the best convergence measure at hand. If too few points are sampled, then a single strike over a densely populated area could shift the aggregate results, indicating that the solution is not yet converged. To establish convergence, the affected population results produced by the model are compared, for a given size range, to the population that would be affected given a uniformly distributed population. Specifically, a running average of the location-specific gridded population counts is compared with a running average of the damage areas multiplied by the average world population density, as a function of the number of impact cases.

Figure 4 shows the population convergence trends for 30 million simulated impacts. The overall results are within ~5% of the average values by 1 million realizations, and are within a fraction of a percent by the full 30 million realizations. Figure 5 shows the average population convergence for four representative size bins within the set: 40-60m, 80-100m, 180-200m, and 280-300m.
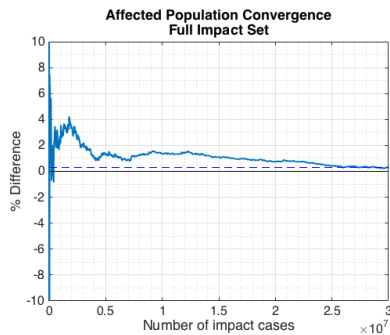

Figure 4: Convergence of the full impact set with all asteroid sizes. The plot shows the percentage difference between a running average of the location-specific gridded population counts and the average population within the average damage area, as a function of number of impact cases.
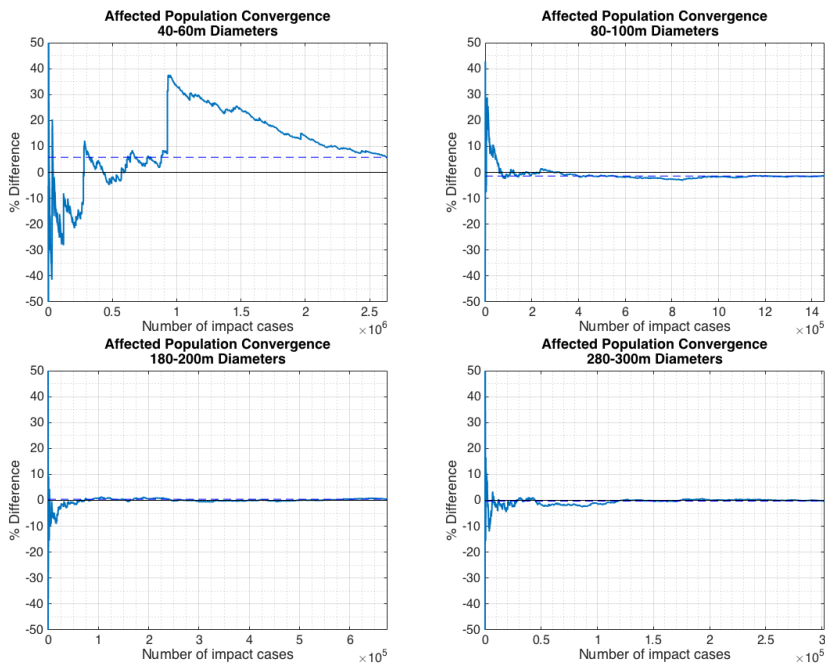
Figure 5: Convergence of local affected population for four size bins within the 30M impact cases. Plots show the percentage difference between a running average of the location-specific gridded population counts and the average population within the average damage area, as a function of number of impact cases. The number of impact cases plotted reflects only the cases sampled within the given size range rather than the total cases in the overall set. The dashed lines show the final value that each bin has converged to over all of cases sampled in this assessment.

As expected, the smallest objects require the most scenarios to converge because the resulting damage areas are the smallest, differ the most based on impact location, and require more points to cover enough overall surface area around the globe. The 40-60m bin, which represents the smallest sizes able to produce statistically notable damage, is within 6% of the average values by the 2.7 million realizations modeled in that size range, while the larger bins are all within ~1% by a few hundred thousand realizations. Overall, these results are sufficiently converged that further variations from additional cases do not noticeably change the ensemble risk results presented.

3.3   Results

A traditional approach to quantifying impact risk involves computing an average expected casualty (E_c) rate for impacts from asteroids up to a given size. In this case, the casualty results from impacts within a given size range are simply averaged and then multiplied by the expected impact frequency for objects of that size. Figure 6 shows an example of the

cumulative expected casualty curve generated from the current impact risk assessment, taking the affected population estimates as the "casualties". The plotted casualty rates represent the cumulative risk from all impacts up to the given size; the cumulative distribution is used to avoid dependence of the results on the size "bins" considered.
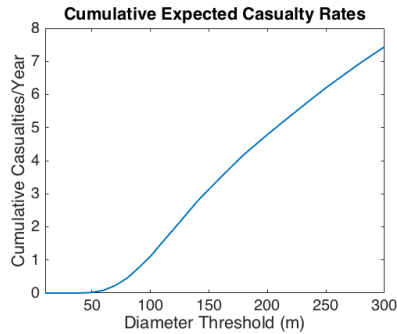

Figure 6: Cumulative expected casualty results (average casualties per year) from asteroids up to a given diameter threshold.

While such an approach seems to provide a very simple cut-and-dry metric for evaluating aggregate risk, it fails to represent the true breadth of risk potential for low-probability, high-consequence events like an asteroid strike. Figures 7 and 8 show the variation in possible outcomes for four asteroid size ranges, assuming an impact occurrence within each size group. These conditional strike results reveal the variation in consequences produced by including uncertain distributions of asteroid impact parameters, prior to accounting for the overall probability of such asteroids striking Earth. Figure 7 shows the relative likelihoods of different affected population ranges for each size. Even when a strike is assumed to occur, the results exhibit a bimodal behavior. The most likely result for any of these sizes is that no population will be affected. However, should the strike occur with consequences, those consequences can become quite severe. For a given impactor size, the severity of the hazard depends significantly on the impact location. Figure 8 compares the min, mean, and max affected population results for the same size ranges, using the local population at specific impact sites vs. assuming an average world population density within the damage areas. While the means naturally remain the same, the maximum consequence levels are an order of magnitude higher when the potential to hit highly populated areas is included. Similarly, even 300-m objects that always produce relatively large damage areas maintain a high probability of striking the ocean and causing no casualties. These important distinctions are lost when distilling results to mean values or using single, representative strike parameters. By using the mean, the range of possible outcomes is completely masked and the full range of information is not represented in an actionable manner.
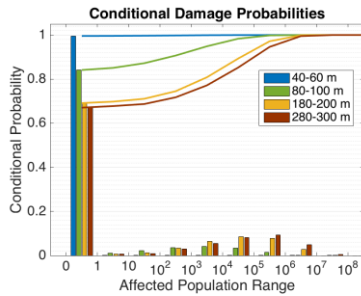
Figure 7: Conditional probabilities of impacts within four size ranges causing varying levels of population damage, given an impact in each size group. The bars represent the relative probabilities of each population range, while the lines represent the cumulative probability up to each range.
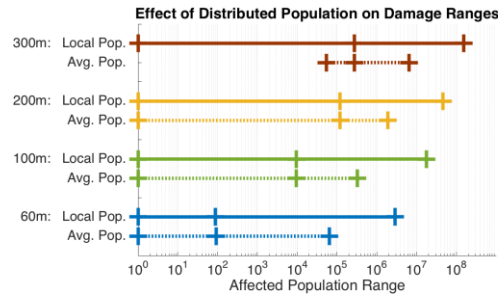
Figure 8. Comparison of the minimum, mean, and maximum affected population consequences given impacts within each size range, assuming either an average world population density (dashed lines) or using local populations at specific impact sites (solid lines).

While Figures 7 and 8 move beyond the simple average outcome, a more complete view of the total risk picture is desired. To this end, Figure 9 shows a contour plot of the likelihood of exceeding various damage levels assuming an impact occurs within each size bin considered. As in Figure 7, these conditional probabilities reflect the range of outcomes stemming from the input parameter distributions and do not account for the frequency with which an impact in that size range may occur. However, rather than giving the relative probabilities of each individual damage range, the exceedance probabilities give the complementary cumulative probability of affecting at least the given population threshold or greater. The use of cumulative probabilities minimizes the arbitrary dependence of the probability values on the width or number of bins selected and instead enables clearer evaluation of meaningful thresholds. Instead of giving a single average value, Figure 9 shows the full range of potential consequences, and their relative likelihoods, given the uncertain variations of asteroid properties and entry parameters.

To assess the absolute level of risk posed by different asteroid sizes, the conditional strike results are then weighted by the likelihood of such impacts occurring. To do this, the estimated annual impact frequency for a given size range, interpolated for each size bin from the values published in [35], is multiplied by the corresponding horizontal slice through Figure 9. In order to avoid the bin-width-dependence that comes with assigning impact probabilities for a given size range, the probabilities are now also presented as cumulative over size as well as damage, representing the probability per year of an impact of a given size or smaller affecting a given population number or higher. The resulting cumulative annual damage exceedance contours are shown in Figure 10.
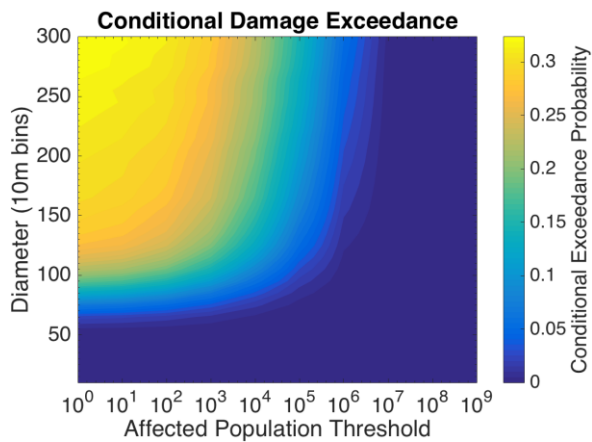
Figure 9: Probability (color contours) that an impact from and asteroid within a given 10-m size range (y-axis) will affect at least a given number of people or more (x-axis), assuming that an impact of that size occurs.
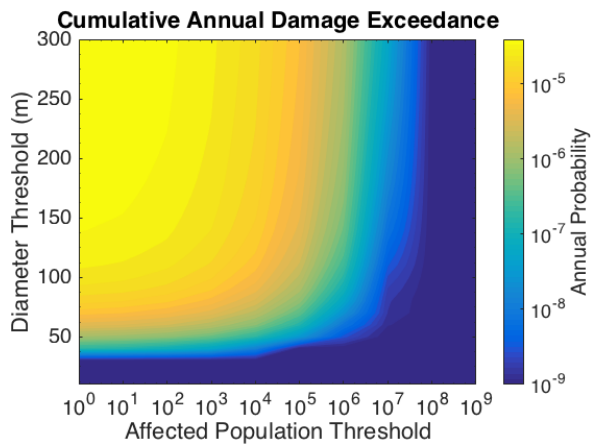

Figure 10: Probability per year (color contours) of an asteroid up to a given size threshold (y-axis) impacting Earth and causing damage that affects at least a given population threshold or more (x-axis).

While Figure 10 presents a complete view of the results, we must next add a risk posture in order to address the question of what size constitutes a considerable threat. In practice, it can be challenging to define a distinct, quantitative risk posture, but for this example it is assumed that the threshold for constituting a threat is a one-in-a-million annual probability of affecting 10,000 people or more. Figure 11 illustrates how the results can provide a size threshold for such a given risk tolerance. The black line shows the one-in-a-million annual probability contour, and the intersecting dashed lines show the size at which the sample

10,000-person threshold exceeds that probability. Based on these assumptions, objects of ~65 m or smaller would not exceed the given risk threshold, while larger objects would be considered to constitute a threat.

In these ways, the cumulative annual damage exceedance figures produced by the PAIR model can provide a full representation of knowledge, or the limits of knowledge, in terms of the uncertainty distribution, while also enabling quantitative answers to be distilled for specific questions.
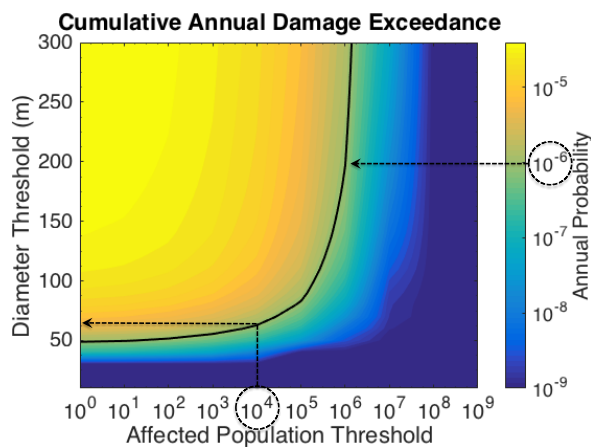

Figure 11: Example of how impact risk probability distributions can provide a size threshold for a sample risk tolerance level of a one-in-a-million probability per year of an impact affecting at least 10,000 people or more. The black line shows the sample 10^{-6} probability contour, and the dashed lines show the minimum asteroid size with that chance of affecting at least 10,000 people.

3.4   Effects of Observational Size Uncertainty on Threat Evaluation

This approach to representing risk uncertainties can further be used to evaluate how different distributions, corresponding to alternate states of knowledge, can influence the answer to the hypothetical size threshold question. Such results can be used to prioritize investments to gain additional knowledge in the context of a threat, or can help characterize the likely limits to the benefit of gaining additional data. As an example, we'll consider a case study looking at how the results change given imperfect knowledge of object diameter.

To investigate the effects of uncertain size estimates based solely on optical observations, the same simulation results shown in Figure 10 are re-binned by an equivalent optical size, calculated from the sampled H-magnitude values and an average albedo of 0.14. In other words, instead of binning the sampled impacts by the actual diameter used in the damage

model, the results are now binned by the diameter which would be estimated from the sampled H-magnitude value and an assumed average albedo. Figure 11 shows the results of this remapping, compared with the direct diameter results adjusted to the same color scale.

The results show that the uncertainty involved with inferring an object diameter based solely on an optical detection lowers the definition of our threat threshold from 65 m to below 20 m. Put another way, an optical system of sizing objects would have to search for objects down to a 20-m equivalent size to capture the same risk exposure as a "perfect" sizing system by detecting objects of 65 m.
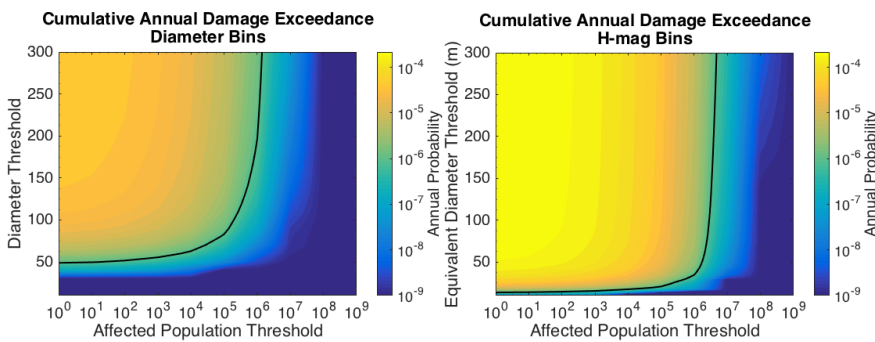

Figure 12: Comparison of risk results based on true asteroid diameters (left) with risk results based on equivalent optical diameter estimates derived from the H-magnitude and an average albedo of 0.14. The black line shows the one-in-a-million probability contour used in the sample risk posture presented in Figure 10.

4.   Conclusions

A new probabilistic asteroid impact risk model was developed to assess the risk that potential asteroid strikes pose to Earth's population. The model consists of a Monte Carlo framework that simulates sets of impact scenarios sampled from distributions describing asteroid and entry characteristics. Including these parameter distributions, along with simulation of the specific entry, breakup, and damage physics for each impact case, enables the results to capture the full range of potential consequences and their likelihoods given different assumptions or levels of knowledge. Such results can be used to bound potential hazard levels for a wide variety of impact scenarios, assess overall ensemble risk from a general asteroid population, and provide insight into what properties or assumptions most significantly affect the potential consequences or risk metrics of interest.

In the current study, 30 million simulated impacts were used to produce a nominal set of ensemble risk results, focusing on mid-sized objects of a few hundred meters or smaller. The results were considered in the context of identifying the minimum asteroid size that constitutes a threat for the given input assumptions. While the average expected casualty rate is the metric typically used to represent the overall threat level, it was argued that this mean measure under-communicates the range of possible outcomes for high-consequence,

low-likelihood events. Instead, the uncertainty distribution results produced by the PAIR model are presented as a richer method of evaluating risk in terms of a threat. A hypothetical risk tolerance level of a one-in-a-million likelihood per year of affecting at least 10,000 people was used to define a minimum impactor size that corresponds to the threat level. For the baseline assumption set in the current analysis, an asteroid diameter of 65 m was the smallest size to constitute that level of threat.

Results were also used to consider the implications of albedo uncertainty in establishing risk metrics for a case where asteroid size is inferred solely based on optical measurement. Instead of characterizing the sampled impacts based on their physical diameter, they were characterized using an equivalent diameter computed based on the sampled H-magnitude and an average assumed albedo of 0.14. For this set of assumptions, the minimum diameter that exceeded the sample risk tolerance level dropped to 20 m. This serves as an example of how use of the entire uncertainty distribution allows for the exploration of questions that depend upon the given state of knowledge. Use of a mean expected casualty value would be ineffectual for assessing the role of these kinds of uncertainties, as all variations would average out. In this way, models such as the one presented here not only provide additional information about the results, but also allow for the exploration of broader questions about how uncertainty in characteristics or modeling assumptions can impact the perceived level of risk and the subsequence research, mitigation, or policy decisions made based on those results.

While the results in this paper focus on the ensemble risk posed by small-to-mid-sized asteroids, the presented approach can also provide valuable risk uncertainty information for a variety of other threat assessment applications. For example, the approach is directly applicable to assessment of a specific impact scenario where the impact location and likelihood are defined from trajectory simulations. Examples of this are the hypothetical impact scenarios presented at conferences [49] [50]. For such assessments, evolving uncertainties about the incoming asteroid properties would drive the range of consequences more significantly as the predicted size and impact location are narrowed. Uncertainty distributions of conditional strike risks can then be used to evaluate and prioritize which asteroid properties are the most critical to determine. Additional ongoing efforts include risk assessments across larger size ranges, accounting for potential global climatic effects and tsunamis generated by large ocean impacts; performance of additional risk sensitivity studies comparing the effects of uncertainties among the various asteroid properties and parameters; and refinement of models or input assumptions in areas that sensitivity studies show to significantly drive the risk results.

References

[1] N. Vasilyev, "The Tunguska Meteorite Problem Today," *Planetary and Space Science*, vol. 46, no. 2, pp. 129-150, February 1998.

[2] D. Barringer, Meteor Crater (formerly called Coon Mountain or Coon Butte) in Northern Central Arizona, November 16, 1909, Paper presented at the National Academy of Sciences, Princeton University.

[3] R. Gersonde et al., "Geological record and reconstruction of the late Pliocene impact of the Eltanin asteroid in the southern ocean," *Nature*, no. 390, pp. 357-363, November 1997.

[4] L. Alvarez, W. Alvarez, F. Asaro, and H. Michel, "Extraterrestrial cause for the Cretaceous-Tertiary extinction," *Science*, no. 208, pp. 1095-1108, 1980.

[5] C. Chapman and D. Morrison, "Impacts on the Earth by Asteroids and Comets: Assessing the hazard," *Nature*, no. 367, pp. 33-39, 1994.

[6] D. Morrison, C. Chapman, and P. Slovic, "The Impact Hazard," in *Hazards Due to Comets and Asteroids*. Tuscon: Univ. of Ariz. Press, 1994, pp. 59-92.

[7] O. Toon, K. Zahnle, D. Morrison, R. Turco, and C. Covey, "Environmental Perturbations Caused by the Impacts of Asteroids and Comets," *Reviews of Geophysics*, vol. 35, no. 1, pp. 41 - 78, 1997.

[8] D. Morrison, "The Spaceguard Survey: Report of the NASA International Near-Earth-Object Detection Workshop," National Aeronautics and Space Administration, Washington D.C.,.

[9] G. Stokes and D. Yeomans, "Study to Determine the Feasibility of Extending the Search for Near-Earth Objects to Smaller Limiting Diameters," National Aeronautics and Space Administration, 2003.

[10] U.S. House. 109th Congress, 1st Session., Public Law 109-155. NASA Authorization Act of 2005., December 30, 2005, Available: https://www.gpo.gov/fdsys/pkg/PLAW-109publ155/pdf/PLAW-109publ155.pdf.

[11] National Research Council, *Defending Planet Earth*. Washington, D.C.: National Academies Press, 2010.

[12] O. Popova et al., "Chelyabinsk Airburst, Damage Assessment, Meteorite Recovery, and Characterization," *Science*, vol. 342, no. 6162, pp. 1069-1073, November 2013.

[13] C. Rumpf, H. Lewis, and P. Atkinson, "On the influence of impact effect modelling for global asteroid impact risk distribution," *Acta Astronautica*, vol. 123, pp. 165-170, June 2016.

[14] S. Motiwala, "An Integrated Physics-Based Risk Model for Assessing the Asteroid Threat," in *Probabilistic Safety Assessment Conference*, 2015.

[15] C. Ericson II, *Hazard Analysis Techniques for System Safety*. Fredericksburg, Virginia: John Wiley & Sons, Inc., 2005.

[16] H. Melosh, "Physical effects of comet and asteroid impacts: Beyond the crater rim," in *Comet/Asteroid Impacts and Human Society*. Berlin: Springer, 2007, pp. 211-224.

[17] M. Boslough and D. Crawford, "Low-altitude airbursts and the impact threat," *International Journal of Impact Engineering*, vol. 35, no. 12, pp. 1441-1448, December 2008, Hypervelocity Impact Proceedings of the 2007 Symposium HVIS 2007.

[18] B. Ivanov, D. Deniem, and G. Neukum, "Implementation of dynamic strength models into 2D hydrocodes: Applications for atmospheric breakup and impact cratering," *International Journal of Impact Engineering*, vol. 20, no. 1-5, pp. 411-430, 1997.

[19] D. Kring, "Air blast produced by the Meteor Crater impact event and a reconstruction of the affected environment," *Meteoritics and Planetary Science*, vol. 32, no. 4, pp. 517-530, July 1997.

[20] C. Chyba, P. Thomas, and K. Zahnle, "The 1908 Tunguska explosion: Atmospheric disruption of a stony asteroid," *Nature*, vol. 361, pp. 40-44, January 1993.

[21] S. Chesley, P. Chodas, A. Milani, G. Valsecchi, and D. Yeomans, "Quantifying the Risk Posed by Potential Earth Impacts," *Icarus*, vol. 159, no. 2, pp. 423-432, October 2002.

[22] C. Chapman, "The hazard of near-Earth asteroid impacts on earth," *Earth and Planetary Science Letters*, vol. 222, no. 1, pp. 1-15, May 2004.

[23] J. Reinhardt, X. Chen, W. Liu, P. Manchev, and M. Pate-Cornell, "Asteroid Risk Assessment: A Probabilistic Approach," *Risk Analysis*, vol. 36, no. 2, pp. 244-261, February 2016.

[24] L. Wheeler, D. Mathias, and P. Register, "A Fragment-Cloud Approach for Modeling Asteroid Breakup and Atmospheric Energy Deposition," 2016, Submitted to Icarus.

[25] P. Register, D. Mathias, and L. Wheeler, "Asteroid Fragmentation Approaches for Modeling Atmospheric Energy Deposition," 2016, Submitted to Icarus.

[26] E. Opik, *Physics of Meteor Flight in the Atmosphere*. Mineola, New York, USA: Interscience, 1958.

[27] J. Hills and M. Goda, "The Fragmentation of Small Asteroids in the Atmosphere," *The Astronomical Journal*, vol. 105, no. 3, pp. 1114-44, 1993.

[28] Q. Passey and H. Melosh, "Effects of Atmospheric Breakup on Crater Field Formation," *Icarus*, vol. 42, pp. 211-233, 1980.

[29] S. Laurence, "Proximal bodies in hypersonic flow," California Institute of Technology, Dissertation (Ph.D) 2006.

[30] J. Hills and M. Goda, "Damage from the impacts of small asteroids," *Planetary and Space Science*, vol. 46, no. 2-3, pp. 219-229, February-March 1998.

[31] M. Aftosmis et al., Numerical Simulation of Bolide Entry with Ground Footprint Prediction, 2016, 54th AIAA Aerospace Sciences Meeting.

[32] S. Glasstone and P. Dolan, "The Effects of Nuclear Weapons," U.S. Government Printing Office, Washington D.C., 1977.

[33] G. Collins, H. Melosh, and R. Marcus, "Earth Impact Effects Program: A Web-based Computer Program for Calculating the Regional Environmental Consequences of a Meteoroid Impact on Earth," *Meteoritics and Planetary Science*, vol. 40, no. 6, pp. 817-840, 2005.

[34] Center for International Earth Science Information Network - CIESIN - Columbia University. (2016) Socioeconomic Data and Applications Center (SEDAC). [Online]. http://dx.doi.org/10.7927/H4639MP

[35] A. Harris, "The population of near-Earth asteroids," *Icarus*, vol. 257, pp. 302–312, September 2015.

[36] A. Mainzer, "Neowise Observations of Near-Earth Objects: Preliminary Results," *The Astrophysical Journal*, vol. 743, no. 2, December 2011.

[37] E. Bowell et al., "Application of photometric models to asteroids," in *Asteroids II; Proceedings of the Conference*, Tuscon, 1988, pp. 524-556.

[38] R. Macke, "Survey of Meteorite Physical Properties: Density, Porosity and Magnetic Susceptibility," Dept. Phys., University of Central Florida, Orlando, FL, PhD Thesis 2010.

[39] T. Spohn, D. Breuer, and T. Johnson, *Encyclopedia of the Solar System*, 3rd ed. Waltham, MA, USA: Elsevier, 2014.

[40] B. Carry, "Density of asteroids," *Planetary and Space Science*, vol. 73, pp. 98-118, December 2012, Provided by the SAO/NASA Astrophysics Data System.

[41] O. Popova et al., "Very low strengths of interplanetary meteoroids and small asteroids," *Meteoritics and Planetary Science*, vol. 46, no. 10, pp. 1525–1550, October 2011.

[42] R. Yoshinaka, M. Osada, H. Park, T. Sasaki, and K. Sasaki, "Practical determination of mechanical design parameters of intact rock considering scale effect," *Engineering Geology*, vol. 96, no. 3-4, pp. 173-186, February 2008.

[43] D. Cotto-Figueroaa et al., "Scale-dependent measurements of meteorite strength: Implications for asteroid fragmentation," *Icarus*, vol. 277, pp. 73-77, October 2016.

[44] S. Greenstreet, H. Ngo, and B. Gladman, "The orbital distribution of Near-Earth Objects inside Earth's orbit," *Icarus*, vol. 217, no. 1, pp. 355-366, January 2012.

[45] W. Bottke et al., "Debiased Orbital and Absolute Magnitude Distribution of the Near-Earth Objects," *Icarus*, vol. 156, no. 2, pp. 399-433, April 2002.

[46] E. Shoemaker, "Interpretation of lunar craters," in *Physics and Astronomy of the Moon*. New York: Academic Press, 283-359.

[47] J. Gallant, B. Gladman, and M. Cuk, "Current bombardment of the Earth-Moon system: Emphasis on cratering asymmetries," *Icarus*, vol. 202, no. 2, pp. 371-382, August 2009.

[48] E. Stern, Personal communication, 2016.

[49] National Aeronautics and Space Administration (NASA). (2015) 2015 PDC Hypothetical Asteroid Impact Scenario. [Online]. http://neo.jpl.nasa.gov/pdc15/

[50] National Aeronautics and Space Administration (NASA). (2017) 2017 PDC Hypothetical Asteroid Impact Scenario. [Online]. http://neo.jpl.nasa.gov/pdc17/

[51] W. Alvarez, P. Claeys, and S.W. Kieffer, "Emplacement of Cretaceous-Tertiary boundary shocked quartz from Chicxulub crater," *Science*, vol. 269, no. 5226, pp. 930-935, August 1995.